Local-disorder-induced low thermal conductivity in degenerate semiconductor Cu22Sn10S32

Ventrapati Pavan Kumar, P. Lemoine, Virginia Carnevali, Gabin Guelou, Oleg I Lebedev, Bernard Raveau, Rabih Al Rahal Al Orabi, Marco Fornari, Christophe Candolfi, Carmelo Prestipino, et al.

▶ To cite this version:

Ventrapati Pavan Kumar, P. Lemoine, Virginia Carnevali, Gabin Guelou, Oleg I Lebedev, et al.. Local-disorder-induced low thermal conductivity in degenerate semiconductor Cu22Sn10S32. Inorganic Chemistry, 2021, 60 (21), pp.16273-16285. 10.1021/acs.inorgchem.1c02105 . hal-03414716

HAL Id: hal-03414716
https://hal.science/hal-03414716v1

Submitted on 20 Jan 2022

Local disorder-induced low thermal conductivity in degenerate semiconductor $Cu_{22}Sn_{10}S_{32}$

Ventrapati Pavan Kumar,[a] *Pierric Lemoine,**[b] *Virginia Carnevali,*[c] *Gabin Guélou,*[a] *Oleg I. Lebedev,*[a] *Bernard Raveau,*[a], *Rabih Al Rahal Al Orabi,*[c] *Marco Fornari,**[c] *Christophe Candolfi,*[d] *Carmelo Prestipino,*[b] *Denis Menut,*[e] *Bernard Malaman,*[d] *Jean Juraszek,*[f] *Koichiro Suekuni,*[g] *Emmanuel Guilmeau**[a]

[a] CRISMAT, CNRS, Normandie Univ, ENSICAEN, UNICAEN, 14000 Caen, France

Email: emmanuel.guilmeau@ensicaen.fr

[b] Univ Rennes, CNRS, ISCR – UMR 6226, F-35000 Rennes, France

Email : pierric.lemoine@univ-rennes1.fr

[c] Department of Physics and Science of Advanced Materials Program, Central Michigan University, Mt. Pleasant, MI 48859, USA

Email: marco.fornari@cmich.edu

[d] Institut Jean Lamour, UMR 7198 CNRS – Université de Lorraine, 2 allée André Guinier-Campus ARTEM, BP 50840, 54011 Nancy Cedex, France

[e] Synchrotron SOLEIL, Ligne MARS, L'Orme des Merisiers, Saint Aubin, 91192 Gif-sur-Yvette, France

[f] GPM, CNRS, Univ Rouen, INSA Rouen, UNIROUEN, 76000 Rouen, France

[g] Interdisciplinary Graduate School of Engineering Sciences, Kyushu University, Kasuga, Fukuoka 816–8580, Japan

Abstract

Sulphur-based semiconductors are attracting attention as environmentally-friendly materials for energy-conversion applications due to their structural complexity and semiconducting properties. Here, we show that the delicate interplay between chemical composition and cationic order/disorder allows to stabilize a new sphalerite derivative phase of cubic symmetry in the Cu-Sn-S diagram: $Cu_{22}Sn_{10}S_{32}$. Interestingly, its crystal structure is characterized by a semi-ordered cationic distribution, the Cu-Sn disorder being localized on one crystallographic site in a long-range ordered matrix. The origin of the partial disorder as well as its influence on the electronic and thermal transport properties are addressed in detail using a combination of synchrotron diffraction, Mössbauer spectroscopy, transmission electron microscopy, theoretical modelling, and transport properties measurements. These measurements evidence that this compound behaves as a pseudo-gap, degenerate *p*-type material with very low lattice thermal conductivity (0.5 W m^{-1} K^{-1} at 700 K). We show that localized disorder is very effective in lowering κ_L without compromising the integrity of the conductive framework. Substituting pentavalent Sb for tetravalent Sn is further exploited to lower the hole concentration and doubles the thermoelectric figure of merit *ZT* to 0.55 at 700 K with respect to the pristine compound. The discovery of this semi-ordered cubic sphalerite derivative $Cu_{22}Sn_{10}S_{32}$ furthers our understanding of the structure-properties relationships in the Cu-Sn-S system and more generally in ternary and quaternary copper-based systems.

Keywords: thermoelectric • sphalerite • disorder • degenerate semiconductor • low thermal conductivity

1. Introduction

Copper tin sulfides (CTS) are an interesting family of compounds with applications in thermoelectricity and photovoltaic. They are mainly p-type conductors formed with non-toxic, eco-friendly, and Earth abundant elements.[1–3] Several CTS with chemical formula $Cu_{2+x}Sn_{1-x}S_3$ have been synthesized to date and have been shown to exhibit attractive electronic and thermal properties: Cu_2SnS_3 ($x = 0$),[1,4] $Cu_7Sn_3S_{10}$ ($x \sim 0.10$),[5] $Cu_5Sn_2S_7$ ($x \sim 0.15$),[6] Cu_3SnS_4 ($x = 0.25$)[7,8]. The thermoelectric performance of these materials, quantified by the dimensionless thermoelectric figure of merit $ZT = S^2T/\rho\kappa$ (T being the operating temperature, S the Seebeck coefficient, ρ the electrical resistivity, and κ the thermal conductivity), is highly dependent on the details of the chemical bonding as well as the cationic distribution in the CTS conductive framework (order-disorder phenomena). For instance, the prototypical Cu_2SnS_3 ($x = 0$) reaches competitive TE performances when doped with Zn and Co, leading to ZT values of 0.58 and 0.85 at 723 K, respectively.[1,4] Although all the aforementioned compounds derive from the ZnS sphalerite structure, they differ from each other by significant structural distortions and cationic orderings which critically influence their transport properties. In several cases, the structural characteristics of different compositions in the CTS family are not clearly established and are subject to controversy in the literature. This is exemplified by the $x = 0$ composition (Cu_2SnS_3), which was reported to be either tetragonal $I\bar{4}2m$ [9] or monoclinic Cc [10] at room temperature, while three polymorphs (cubic $F\bar{4}3m$, tetragonal $I\bar{4}2m$, and monoclinic Cc) were found to coexist for $0.016 \leq x \leq 0.08$.[11] Importantly, many Cu-Sn-S samples were reported to crystallize in the kuramite type tetragonal ($I\bar{4}2m$) structure,[9,12–14] with various chemical compositions and various cationic distributions on the crystallographic sites. A common structural feature is that each model assigns mixed occupancy of the $2b$ and $4d$ sites by Cu and Sn atoms, while the $2a$ site is solely occupied by Cu atoms. Most of the descriptions correspond to an almost equivalent occupation of the 2*b* and 4*d* sites by Cu and Sn atoms, leading to disordered cationic arrangement. This is the case, for instance, of Cu_2SnS_3 ($x = 0$) that was reported by Chen *et al.* as $Cu_{2.67}Sn_{1.33}S_4$.[9] In fact, the authors determined that the 2*b* and 4*d* sites show mixed occupancies of Cu and Sn atoms (~55% and ~45%, respectively). Otherwise, some studies reported on preferential occupation of the 2*b* and 4*d* sites by Sn and Cu atoms, leading to more ordered arrangement, as in the case of the $x \sim 0.10$ compound, reported as $Cu_7Sn_3S_{10}$[5]. In this study, based on the analysis of X-ray powder diffraction (XRPD) data, Deng *et al.* considered that Cu and Sn atoms mainly occupy the 4*d* and 2*b* site (82%), respectively, based on the analysis of powder XRD data. However, this conclusion is questionable since the final refined tin content was significantly lower than the nominal value. To override this ambiguity, the authors decided to fix the site occupancies in accordance with the nominal composition.

In a recent investigation of the $Cu_{2+x}Sn_{1-x}S_3$ system, a perfectly ordered sphalerite derivative phase, $Cu_5Sn_2S_7$, with a monoclinic $C2$ structure, was synthesized for $x = 0.15$.[6] This phase, isotypic to both $Cu_4NiSi_2S_7$,[15] and the homologous selenide $Cu_5Sn_2Se_7$,[16] was shown to be, unlike other compositions, a degenerate semiconductor with a high carrier mobility. For an intermediate composition, $x = 0.075$ ($Cu_{2.075}Sn_{0.925}S_3$), a pure phase was identified,[6] and similarly to the $x \sim 0.10$ phase reported by Deng et al., [5] can be apparently indexed in the tetragonal space group of kuramite ($I\bar{4}2m$). As in the case of $Cu_5Sn_2S_7$, the phase $Cu_{2.075}Sn_{0.925}S_3$ was also shown to be a degenerate semiconductor with remarkably low thermal conductivity, leading to a significantly higher *ZT* value of 0.30 at 700 K compared to the former (*ZT* = 0.10 at 700 K).[6] Similarly to the $x \sim 0.10$ phase reported by Deng *et al.*,[5] the XRPD pattern of the $x = 0.075$ sample can be refined by considering a kuramite structural model ($I\bar{4}2m$) but leads to important deviation of the refined chemical composition compared to the nominal one. This suggests that, in addition to the Cu/Sn ratio, the crystal structure plays a crucial role in the thermoelectric properties of these sphalerite derivatives. Intrigued by the low lattice thermal conductivity, we revisited $Cu_{2.075}Sn_{0.925}S_3$ and found anomalies in the XRPD data results when refining with the kuramite structural model ($I\bar{4}2m$). Reasonably high quality Rietveld refinements can be achieved by considering the structural model proposed by Deng *et al*. for $x \sim 0.10$.[5] However, all the compositional refinements lead to much lower tin content than that of the nominal composition $Cu_{2.075}Sn_{0.925}S_3$. This indicates that alternative structural models must be considered for the composition range between $x = 0.06$ and $x = 0.15$. Our detailed reinvestigation points to a cubic symmetry sphalerite derivative phase of chemical composition $Cu_{22}Sn_{10}S_{32}$ ($x = 0.063$), whose lattice parameter $a_c \sim 10.5$ Å is closely related to those of the tetragonal kuramite, $a_c = c_T = 2a_T$, but implying a crystal structure partially-disordered with space group $P\bar{4}3n$. Interestingly, the cationic disorder is restricted to only one crystallographic site within the ordered sphalerite matrix but, nonetheless, influences dramatically the lattice thermal conductivity of this material.

In the next sections, the careful characterization of the crystal structure, the analysis of the electronic and vibrational density of states with first principles calculations, and the assessment with theory and experiments of the microscopic interplay observable in the transport coefficients are presented for the first time. Guided by those results, we have further investigated the beneficial role of Sb doping in decreasing the hole concentration to improve dramatically the electronic transport properties and reach competitive *ZT* values.

2. Experimental Section

Materials Synthesis

The polycrystalline sample of Cu_2SnS_3 was synthesized by a two-step solid state reaction in evacuated silica tubes from the elemental precursors (Cu (99%, Alfa Aesar), Sn (99.85%, Alfa Aesar), and S (99.5%, Alfa Aesar)). First, Cu, Sn and S were ground in an agate mortar with the appropriate stoichiometric ratio and compacted into a pellet, sealed in an evacuated silica tube and heated to 1023 K at a rate of 50 K min^{-1}. The pellet was held at that temperature for 48h followed by a cooling step down to room temperature at a rate of 50 K min^{-1}. Subsequently, the as-prepared Cu_2SnS_3 sample was crushed and the powder was compacted for a second firing carried out at 873 K for 24h with an intermediate step at 673 K for 12h. The same heating and cooling rates of 50 K min^{-1} were used. The obtained sample was once again ground and sieved down to 200 µm to remove large agglomerates.

$Cu_{2+x}Sn_{1-x}S_3$ (x = 0.075, 0.1, 0.125, and 0.15) and $Cu_{22}Sn_{10-y}Sb_yS_{32}$ (y = 0, 0.75, and 1.0) samples were synthesized by mechanical-alloying. All sample preparations and handling of powders were performed in an argon filled glovebox with oxygen content <1 ppm. Stoichiometric amounts of high purity elements Cu (99%, Alfa Aesar), Sn (99.85%, Alfa Aesar), Sb (99.5%, Alfa Aesar) and S (99.5%, Alfa Aesar) were loaded in a 25 mL tungsten carbide jar containing 7 balls of 10 mm under argon atmosphere. High-energy ball-milling was performed in a Fritsch Pulverisette 7 Premium line planetary ball-mill operating at room temperature (RT) at a disc rotation speed of 600 rpm during 6 h. The resulting powders were then ground and sieved down to 150 µm.

The obtained powders of $Cu_{2+x}Sn_{1-x}S_3$ (x = 0, 0.075, 0.1, 0.125, and 0.15) compositions were then placed in a graphite die of 10 mm diameter and densified by SPS (FCT HPD 25) at 873 K for 30 min under a pressure of 64 MPa (heating and cooling rate of 50 and 20 K min^{-1}, respectively). Powders of $Cu_{22}Sn_{10-y}Sb_yS_{32}$ (y = 0, 0.75, and 1.0) compositions were densified at 823 K for 30 min under a pressure of 64 MPa. The final dimensions of the pellet are around 8 mm in thickness and 10 mm in diameter. Relative densities are about 91-92% for $Cu_{2+x}Sn_{1-x}S_3$ ($x = 0.075, 0.1, 0.125$, and 0.15) samples and > 95% for Cu_2SnS_3 and $Cu_{22}Sn_{10-y}Sb_yS_{32}$ ($y = 0, 0.75$, and 1.0) samples.

X-ray powder diffraction

X-ray powder diffraction (XRPD) data were collected at room temperature using a Bruker D8 Advance Vario 1 two-circle diffractometer (θ-2θ Bragg-Brentano mode), equipped with a Ge(111) monochromator (Johansson type) and a Lynx Eye detector, using Cu $K\alpha_1$ radiation ($\lambda = 1.5406$ Å). Synchrotron XRPD data of $Cu_{2.075}Sn_{0.925}S_3$ sample was collected at room temperature on the end-station CX2 devoted to the high-resolution XRD measurements of MARS (Multi-Analysis On Radioactive Samples) beamline at SOLEIL synchrotron (Saint-Aubin, France). The beamline uses a bending magnet source and the X-rays are monochromatized by a double crystal monochromator (DCM) equipped with a pair of Si(220) crystals. The second crystal is sagittally bent to perform the horizontal beam focusing. Higher harmonics rejection and vertical collimation were achieved using the Pt strip of the two mirrors inserted before and after the DCM with a 3.1 mRad incidence angle. The incident X-ray energy was calibrated using the absorption K-edge of an Y foil ($E_0 =$ 17.038 keV) with a beam sizing about 1000×300 μm (H×V) at the sample position. The station is equipped by an angular precision two-circle goniometer for the collection of powder diffraction in Debye-Scherrer geometry. High-resolution data was carried out by the use of a set of 24 detectors equipped with crystal analyzer Ge(111).[17] Sample was finely ground and inserted in a boron glass capillary of diameter 0.3 mm in order to avoid the necessity to correct the data for absorption. The analysis of the diffraction patterns was performed by Rietveld refinement using the FullProf and WinPlotr software packages.[18,19] Background contribution was estimated either manually or using a polynomial function. Zero-point shift, lattice parameters, peak shape parameters and asymmetry parameters were systematically refined. Fractional atomic coordinates and isotropic displacement parameters (*i.e.* Debye-Waller factors B_{iso}) were refined for samples free of the monoclinic $C2$ $Cu_5Sn_2S_7$ phase, i.*e.* $Cu_{2.075}Sn_{0.925}S_3$ and $Cu_{22}Sn_{10-y}Sb_yS_{32}$ (y = 0, 0.75 and 1).

Single-crystal X-ray diffraction

Single-crystal X-ray structural analysis of $Cu_{22}Sn_{10}S_{32}$ compound was carried out at 296 K on APEX II Bruker AXS diffractometer, using Mo-Kα X-ray wavelength (λ = 0.71073 Å) at the Centre de DIFfractométrie X (CDIFX) de l'Institut des Sciences Chimiques de Rennes. The structures were solved by direct methods using the SIR97 program,[20] and then refined will full-matrix least-square methods based on F^2 (SHELXL-2014)[21] through the aid of the WinGX platform.[22] The chemical composition was fixed to that determined by synchrotron X-ray diffraction analysis and confirmed by scanning electron microscopy with energy dispersive spectroscopy (SEM-EDS) measurements performed at the Centre de Microscopie Electronique à BAlayage (CMEBA), platform of the ScanMAT unit, UMS 2001, of the University of Rennes 1, using a JEOL IT 300 LA microscope equipped with a EDS SDD detector and calibrated using single-crystals of $Cu_4Sn_7S_{16}$. All atoms were refined with anisotropic atomic displacement parameters. The conditions of data collection and structure refinements are gathered in **Table 2** and the refined crystallographic data in **Table S1**. Interatomic distances and bond angles are gathered in **Table S2**.

Transmission electron microscopy

HAADF-STEM, ED studies, and EDXSTEM were performed on JEM ARM200F cold FEG double aberration-corrected microscope operated at 200 kV and equipped with ORIUS CCD camera, large angle CENTURIO EDX detector, and GIF QUANTUM.TEM specimen was prepared by grinding the material in agate mortar in ethanol and depositing suspension on Ni carbon holey grid.

Electrical and thermal properties measurements

The electrical resistivity (ρ) and Seebeck coefficient (S) were measured simultaneously from 300 K up to 700 K on bar-shaped samples of typical dimensions 2×3×10 mm^3 using an ULVAC-ZEM3 instrument under partial helium pressure. A NETZSCH LFA-457 apparatus was used for measuring the thermal diffusivity under argon flow. The thermal conductivity (κ) was determined as the product of the geometrical density, the thermal diffusivity, and the theoretical heat capacity using the Dulong−Petit approximation. Heat capacity (Cp) measurements have been performed on $Cu_{22}Sn_{10}S_{32}$ and $Cu_{22}Sn_9Sb_1S_{32}$ samples to confirm the agreement between experimental and Dulong-Petit approximation values (**Figure S1**). The lattice contribution to the thermal conductivity (κ_L) was determined by subtracting the estimated electronic component (κ_e) from the measured total thermal conductivity, κ. The measurement uncertainties are estimated to be 6% for the Seebeck coefficient, 8% for the electrical resistivity, 11% for the thermal conductivity, and 16% for the final dimensionless figure of merit, ZT.[23]

An initial assessment of the thermal stability and the reproducibility of the thermoelectric properties of $Cu_5Sn_2S_7$ were carried out through TG/DSC (**Figure S2**) and cycling measurements of the electrical transport properties, up to 650 K (**Figure S3**) and 700 K (**Figure S4**). No significant mass loss and decomposition/crystallization phenomena are observed for both compounds up to 700 K. Cycling measurements results show that, up to 650 K, $Cu_{22}Sn_{10}S_{32}$ remains stable with no systematic variation in the performances, all being within the experimental uncertainty. There are very small but systematic variations of the transport coefficient during the stability experiment up to 700 K. Although the overall performance is not significantly affected, the systematic decrease in the Seebeck coefficient may indicate some changes in the materials. The exact nature of these changes will require further experimental investigation.

Hall effect measurements over the temperature range of 5 K to 300 K were carried out using a Physical Properties Measurement System (PPMS; Quantum Design) under an applied magnetic field of 9T. Electrical resistivity, Seebeck coefficient and thermal conductivity were simultaneously measured over the temperature range of 5 K to 300 K using the thermal transport option (TTO) of the PPMS. Indium contacts were used.

Transverse and longitudinal sound velocities were measured at room temperature by a pulse-echo technique with piezoelectric transducers on a small piece of the consolidated pellets. A tiny amount of honey was used to ensure a good contact between the sample and the transducers.

First principles calculations

All the calculations were computed using the quantum ESPRESSO[24] package as incorporated in the high-throughput infrastructure of AFLOW π .[25] Optimized norm-conserving PBE pseudopotentials,[26] well converged basis sets corresponding to an energy cutoff of 150 Ry for the wave functions and 600 Ry for the charge density, and ACBN0 functional approach[27] have been used to self-consistently determine the values for the Hubbard corrections for each atomic species of the material. To integrate over the Brillouin zone, a $4 \times 4 \times 4$ (shifted) grid was used. The phonon calculations use ultrasoft PBE pseudopotentials[28] (energy cutoff of 60 Ry and a $4 \times 4 \times 4$ (shifted) grid). Seebeck coefficient S and electrical conductivity σ were computed by solving Boltzmann transport equation within the constant relaxation time and the rigid band approximation as implemented in PAOFLOW.[29]

3. Results and discussion

3.1. Structure analysis in the $Cu_{2+x}Sn_{1-x}S_3$ series ($0.075 \leq x \leq 0.15$)

In order to determine the crystal structure of the $Cu_{2.075}Sn_{0.925}S_3$ phase, synchrotron X-ray powder diffraction (XRPD) data have been recorded. As previously mentioned, apparent high quality Rietveld refinement (**Figure S5**) obtained with a kuramite structural model (**Figure S6**) suggests in a first approach that the $x = 0.075$ sample crystallizes in a tetragonal structure. The analysis provides (i) a c_T/a_T ratio of 2, (ii) a preferential occupation of the 2*b* site by Sn atoms (73.4%) and of the 4*d* sites by Cu atoms (95.5%), and (iii) a cationic distribution corresponding to the chemical composition of $Cu_{3.18}Sn_{0.82}S_4$, *i.e.* $Cu_{2.38}Sn_{0.62}S_3$ ($x = 0.38$ in the generic formula $Cu_{2+x}Sn_{1-x}S_3$). This Sn content strongly differs from the nominal composition $x = 0.075$. In addition, according to our previous study,[6] this proposed concentration of $x = 0.38$ is in disagreement with the very narrow composition window allowing for the stability of this phase. In fact, a higher (Cu_2SnS_3) and lower ($Cu_{2.15}Sn_{0.85}S_3$) tin content compared to $Cu_{2.075}Sn_{0.925}S_3$ leads to the formation of the mohite Cu_2SnS_3 phase (Cc space group) and the $Cu_5Sn_2S_7$ phase ($C2$ space group), respectively. A value as high as $x = 0.38$ should induce the formation of Sn-rich secondary phases in the sample. This is the case, for instance, for $x = 0.1$ (reported by Deng *et al.* as single phase $Cu_7Sn_3S_{10}$)[5] and $x = 0.125$ samples, both characterized by a mixture of the title phase $Cu_{22}Sn_{10}S_{32}$ and $Cu_5Sn_2S_7$ (**Figure S7**). Consequently, the structural model of kuramite is not compatible with the $x = 0.075$ phase. The fact that the c_T/a_T ratio is equal to 2 suggests that the $Cu_{2.075}Sn_{0.925}S_3$ phase could crystallize in a cubic unit cell ($a_c = 2a_T$). This is supported by the existence of a weak intensity diffraction peak, detected at $2\theta = 9.44°$ on the synchrotron XRPD pattern (λ = 0.7273 Å). Such a feature is not compatible with the tetragonal unit cell (**Figure S5 and S6)** but can be indexed by a cubic unit cell with a_c = 10.8234(2) Å (**Figure 1**), equivalent to four tetragonal unit cells (*i.e.* $a_c = 2a_T = c_T$). The presence of the reflections hkl with $h+k = 2n+1$, $h+l = 2n+1$, and $k+l = 2n+1$ allows to exclude a face-centered lattice and of those with $h+k+l = 2n+1$ a body-centered lattice. Moreover, the systematic absence of the reflections hhl with $l = 2n+1$, hkh with $k = 2n+1$, and hkk with $h = 2n+1$ indicates the presence of n glide planes perpendicular to <100> set directions. Finally, the presence of reflections $0kl$ with $k + l = 2n+1$, $h0l$ with $h + l = 2n+1$, and $hk0$ with $h + k = 2n+1$ indicates the absence of n glide planes perpendicular to <011> set directions. From these condition analyses, the possible cubic space groups are either $P\bar{4}3n$ or $Pm\bar{3}n$. However, from spectroscopy techniques (Mössbauer and XAS), it is shown that this phase is a sphalerite derivative representative,[6] allowing to exclude the centrosymmetric space group $Pm\bar{3}n$, leaving $P\bar{4}3n$ as the only possible solution.

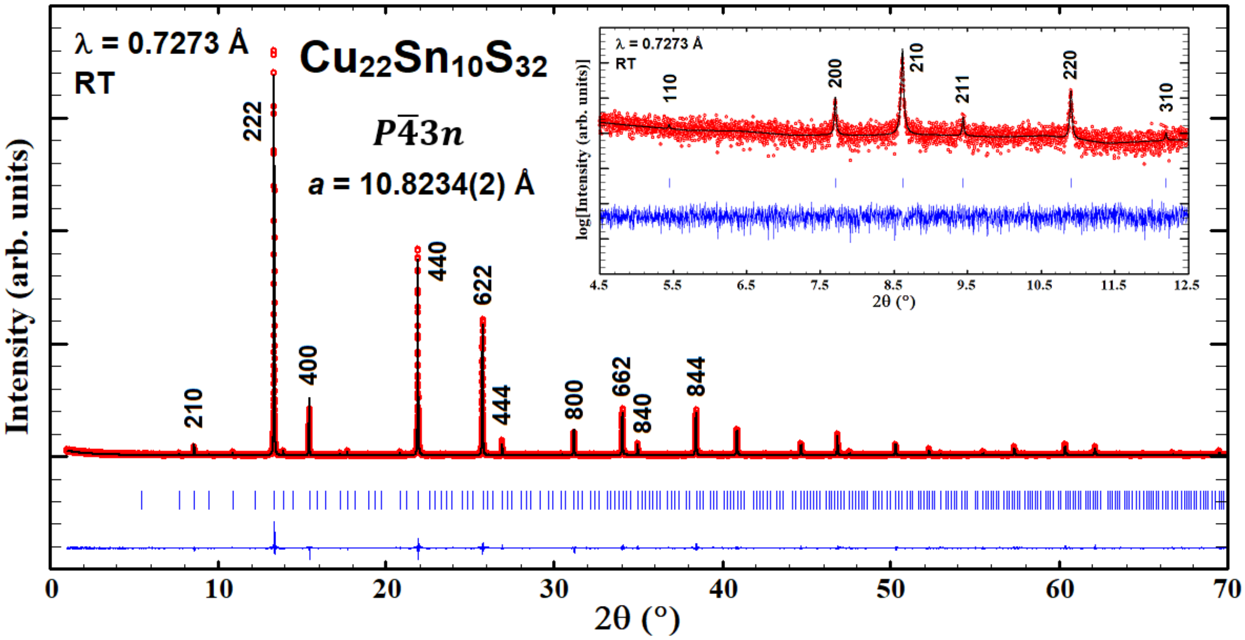

Figure 1. Synchrotron XRPD Rietveld refinement of the $Cu_{2.075}Sn_{0.925}S_3$ sample corresponding to the $Cu_{22}Sn_{10}S_{32}$ phase.

The structural similarities (space group and unit cell parameter) between this $Cu_{2.075}Sn_{0.925}S_3$ phase and the colusite $Cu_{26}V_2Sn_6S_{32}$, led us to consider a structural model derived from that of colusite. Nevertheless, considering that the cation over sulphur ratio is expected to be equal to 1 for the $Cu_{2.075}Sn_{0.925}S_3$ phase, the 2*a* crystallographic site (known as the “interstitial” site in colusite) was kept empty in the structural model. Hence, we have considered that Cu and Sn atoms should be distributed on 6*c*, 6*d*, 8*e*, 12*f* sites, and S atoms should be located on 8*e* and 24*i* sites. As clearly shown on the synchrotron XRPD patterns (**Figure 1, Figure S8**), the strong intensity of the *hkl* reflections with $h+k+l = 2n+1$ suggests an important chemical contrast between 6*c* and 6*d* sites. From these considerations, we have started the crystal structure resolution of the $Cu_{2.075}Sn_{0.925}S_3$ phase by considering (i) the structural model of colusite, (ii) an empty 2*a* site, and (iii) Sn and Cu atoms on the 6*c* and 6*d* sites, respectively. This starting model requires considering a possible mixture of Cu and Sn either on the 8*e* site, or 12*f* site, or on both sites. High quality Rietveld refinement was finally reached for an occupation of the *12f* site by Cu (~2/3) and Sn (~1/3), the 8*e* site being fully occupied by Cu atoms. This suggests that the structural formula of the $Cu_{2.075}Sn_{0.925}S_3$ phase is close to $Cu_{22}Sn_{10}S_{32}$. The crystallographic data of the $Cu_{22}Sn_{10}S_{32}$ phase, obtained from Rietveld refinement of the synchrotron XRPD pattern recorded at room temperature, are gathered in **Table 1**. Note that contrary to the tetragonal kuramite model, this new cubic structural model leads to a refined chemical composition, corresponding to $x = 0.0625$ (*i.e.* $Cu_{2.0625}Sn_{0.9375}S_3$), in agreement with the nominal one.

Table 1. Crystallographic data of the $Cu_{22}Sn_{10}S_{32}$ phase from Rietveld refinement of the synchrotron XRPD pattern recorded at room temperature.

$P\bar{4}3n$, *a* = 10.8234(2) Å, $Cu_{21.8(1)}Sn_{10.2(1)}S_{32}$

Atom label	Site	x	y	z	Biso (Å^2)	SOF
Sn1	6c	1/4	1/2	0	0.72(4)	1.00
Cu2	6d	1/4	0	1/2	0.41(6)	1.00
Cu3	8e	0.249(2)	x	x	0.90(5)	1.00
Cu4/Sn4	12f	0.248(1)	0	0	1.34(7)	0.65(1)/0.35(1)
S1	8e	0.126(1)	x	x	1.21(34)	1.00
S2	24i	0.376(1)	0.367(1)	0.128(1)	0.11(8)	1.00

3.2. Transmission Electron Microscopy Study of the $Cu_{2.075}Sn_{0.925}S_3$ sample

In order to confirm the structural model and to check the homogeneity of the sample, transmission electron microscopy (TEM) analyses were performed. Electron diffraction (ED) patterns collected along the main zone axis (**Figure 2a**) clearly confirmed the cubic $P\bar{4}3n$ structure with a unit cell parameter a_c ~ 10.5 Å, in agreement with the synchrotron XRPD study. EDX–STEM elemental mapping (**Figure 2a** bottom panels) shows a homogeneous distribution of all the elements. The quantitative analysis carried out for tens of crystallite gives the following composition Cu-37.9, Sn-17.2, S-44.9 at.%, which is close to the expected chemical composition.

HAADF-STEM images evidence the good crystallinity of the sample that is free of any structural modulation and defects. This is illustrated by the high resolution [001] HAADF-STEM image (**Figure 2b**). The simulated HAADF-STEM image based on the proposed cubic $P\bar{4}3n$ structure confirms the partially ordered character of the structure, where pure [001] Cu (Z = 29, less brightness dots) and Sn (Z = 50, brightest dots) columns alternate with mixed Sn/Cu columns (bright dots) in agreement with the experimental image.

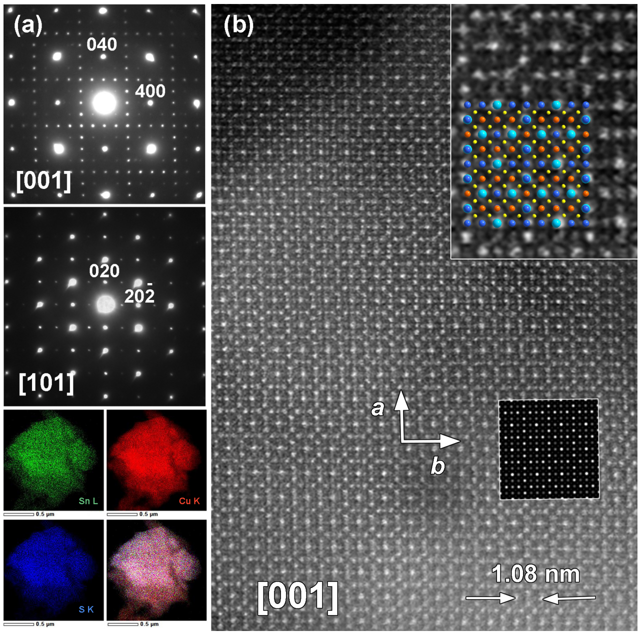

Figure 2. a) ED patterns along main crystallographic zone axes of cubic $Cu_{22}Sn_{10}S_{32}$ structure indexed based on $P\bar{4}3n$ space group (a = 10.52 Å) and EDX-STEM colour elemental mapping for Sn L (green) Cu K (red), S K (blue) and overlaid image. b) High resolution [001] HAADF-STEM image of cubic $Cu_{22}Sn_{10}S_{32}$. The simulated and magnified image together with overlaid structural model are given in the inset (Sn- light blue, Sn/Cu – dark blue, Cu – orange, S- yellow).

3.3. Single crystal X-ray diffraction

The space group and the structural model described above were confirmed by single-crystal XRD analysis. Single-crystals were extracted from a powder sample $Cu_{2.075}Sn_{0.925}S_3$ prepared by conventional synthesis in sealed silica tube and analyzed by XRD and SEM-EDS. The chemical composition of $Cu_{21.7(7)}Sn_{9.8(5)}S_{32.5(10)}$, determined from SEM-EDS analyses using single-crystals of $Cu_4Sn_7S_{16}$ ($Cu_{3.9(2)}Sn_{6.9(3)}S_{16.2(5)}$) as standard compound, is in excellent agreement with the chemical formula refined from synchrotron XRPD data. This composition was then used for the final refinement of the single-crystal XRD data. The weak residual electronic density determined from the refinement suggests that no atoms are located at “interstitial” position of the sphalerite framework. The conditions of data collection and structure refinement are summarized in **Table 2** and the refined crystallographic data in **Table S1**.

Table 2. Summary of single-crystal data collection and structure refinement conditions at room temperature of the $Cu_{22}Sn_{10}S_{32}$ compound

Structural formula	$Cu_{22}Sn_{10}S_{32}$
Space group	$P\bar{4}3n$
Temperature (K)	296(2)
Formula weight (g mol^{-1})	3610.70
Wavelength (Å)	0.71073
Crystal system	cubic
a (Å)	10.8925(18)
V (Å^3)	1292.4(6)
Z	1
Calculated density (g cm^{-3})	4.639
Absorption coefficient (mm^{-1})	14.863
F(000)	1650
Crystal size (mm)	0.06×0.05×0.04
Crystal color	grey
Theta range (°)	2.644-33.087
h_min, h_max	0, 11
k_min, k_max	0, 11
l_min, l_max	1, 16
R(int)	0.1118
Reflections collected	1236
Reflections unique [$I > 2\sigma$]	345
Completeness	1.000
Data/restraints/parameters	1236/0/27
Goodness-of-fit	0.946
Final R_1 [$I > 2\sigma$]	0.0759
Final wR_2 [$I > 2\sigma$]	0.1400
Largest difference peak and hole (e Å^{-3})	1.015/-1.178

The interatomic distances in the cubic $Cu_{22}Sn_{10}S_{32}$ phase, calculated from the Rietveld refinement of the synchrotron XRPD data and from the refinement of the single-crystal XRD data, are gathered in **Table 3** and **Table S2**, respectively. These values are in agreement with those encountered in sphalerite derivative copper sulfides, *i.e.* 2.30 Å for Cu-S and 2.43 Å for Sn-S.[6] Moreover, the average interatomic distances of 2.36 Å determined between metals on the 12*f* site (*i.e.* M4) and S atoms, intermediate between Cu-S and Sn-S distances, confirm the occupation of the site by both Cu and Sn atoms. Compared to the monoclinic Cu_2SnS_3 and $Cu_5Sn_2S_7$ phases,[6,10] the bond angles values do not differ significantly from the ideal angle of tetrahedron, indicating a weakly distorted sphalerite framework in $Cu_{22}Sn_{10}S_{32}$. Nevertheless, the ^{119}Sn Mössbauer ΔE_Q value of 0.90 mm s^{-1} reported for this cubic phase,[6] intermediate between those of the monoclinic Cu_2SnS_3 and $Cu_5Sn_2S_7$ phases, suggests a non-negligible local disorder of the sphalerite framework induced by the mixed occupancy of the 12*f* crystallographic site. As aforementioned, the original crystal structure of the cubic sphalerite derivative $Cu_{22}Sn_{10}S_{32}$ phase, shown in **Figure 3**, is related to that of $Cu_{26}V_2Sn_6S_{32}$ colusite with however two main differences: (i) the absence of atoms in the "interstitial" position and (ii) the occupancy of the 12*f* site by a mixture of Cu and Sn atoms. The former point implies the absence of tetrahedral-octahedral complexes $[TS_4]Cu_6$, a structural feature of prime importance that controls the thermoelectric properties of colusites. The latter point confirms a cubic sphalerite derivative phase with a partially ordered structure, a structural feature at the origin of its low lattice thermal conductivity discussed below.

These structural results definitely demonstrate the existence of a new partially ordered cubic sphalerite $Cu_{22}Sn_{10}S_{32}$ ($x = 0.063$) for a narrow compositional range around $x = 0.06$-0.075 in the $Cu_{2+x}Sn_{1-x}S_3$ system. As a consequence, the unsatisfactory structure refinements obtained by Deng et *al* [4] for $x = 0.10$ suggest that the existence of the phase $Cu_7Sn_3S_{10}$ with a tetragonal I-*42m* structure reported by these authors is questionable.

Table 3. Interatomic distances (Å) and bond angles (°) in $Cu_{22}Sn_{10}S_{32}$ ($x = 0.063$, space group $P\bar{4}3n$) from Rietveld refinement of the room temperature synchrotron XRPD pattern.

Sn1-S2 ×4	2.421(6)	S2-Sn1-S2 ×4	108.6(2)
Cu2-S2 ×4	2.304(6)	S2-Sn1-S2 ×2	111.2(2)
Cu3-S1	2.312(20)	S2-Cu2-S2 ×4	107.6(2)
Cu3-S2 ×3	2.291(19)	S2-Cu2-S2 ×2	113.4(2)
M4-S1 ×2	2.334(9)	S1-Cu3-S2 ×3	109.8(8)
M4-S2 ×2	2.382(6)	S2-Cu3-S2 ×3	109.1(8)
$\overline{d_{M4-S}}$	2.358	S1-M4-S1	110.9(4)
		S1-M4-S2 ×2	107.2(3)
		S1-M4-S2 ×2	110.2(3)
		S2-M4-S2	111.2(2)

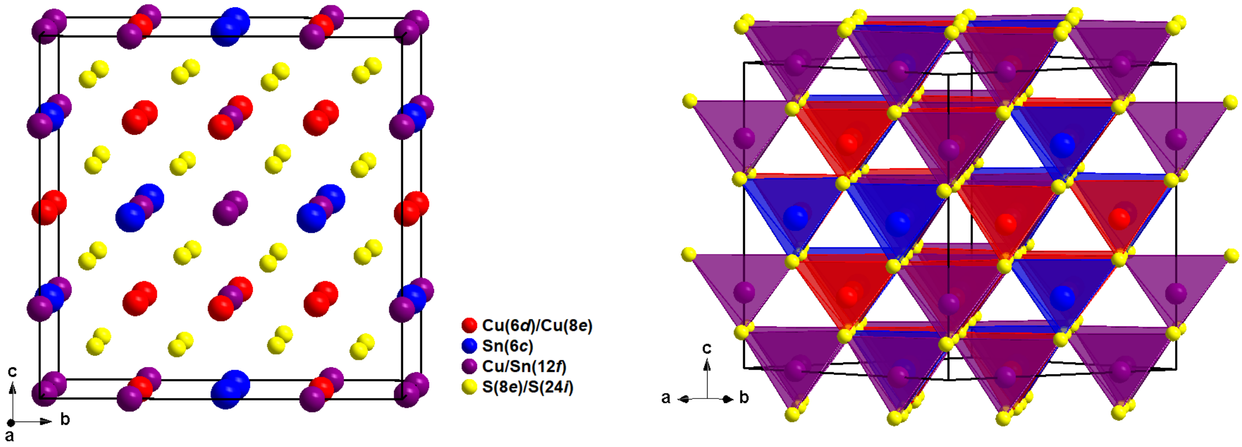

Figure 3. Crystal structure representations of the cubic sphalerite derivative semi-ordered phase $Cu_{22}Sn_{10}S_{32}$.

3.4. Low temperature transport properties

Figure 4a and 4b show the electrical resistivity and Seebeck coefficient as a function of temperature from 5 to 300 K. For comparison purposes, the data measured on Cu_2SnS_3 and $Cu_{2.15}Sn_{0.85}S_3$ (reported as $Cu_5Sn_2S_7$) samples have been included. Compared to the stoichiometric parent compound Cu_2SnS_3 that exhibits nearly-intrinsic semiconducting properties, an increase in the Cu-to-Sn ratio results in a progressive shift towards a highly-degenerate p-type semiconducting behavior. This enhanced metallicity is in agreement with electron counting rules, which predict that the partial substitution of Cu^+ for Sn^{4+} leads to the formation of free holes in the valence band. Consistently, the electronic properties of the x = 0.075 sample are intermediate between the semiconducting x = 0 and heavily doped x = 0.15 samples. This trend is further supported by Hall effect measurements that evidence a significant increase in the hole concentration p_H from approximately 2.2×10^{17} cm^{-3} in Cu_2SnS_3 to 4.70×10^{21} cm^{-3} for x = 0.075 and to 5.75×10^{21} cm^{-3} for x = 0.15 at 300 K. The weak temperature dependence of p_H upon cooling to 5 K for x = 0.075 and x = 0.15 (reported as $Cu_5Sn_2S_7$) samples is consistent with their degenerate behavior (**Figure S9**). The influence of the partial structural disorder characterizing the x = 0.075 sample is highlighted by the temperature-dependent behaviors and magnitudes of the Hall mobility μ_H, shown in **Figure S10**. At 5 K, μ_H shows a fifteen-fold increase on going from x = 0.075 to x = 0.15, reaching 8.8 cm^2 V^{-1} s^{-1} and 140 cm^2 V^{-1} s^{-1}, respectively. Of note, for x = 0.075, μ_H decreases with increasing temperature, approximately following a $T^{-1/2}$ dependence indicative of alloy scattering, a mechanism typically observed in solid solutions and strongly off-stoichiometric compounds.[30–32] This result is consistent with the semi-ordering cationic arrangement in this compound compared to its two monoclinic counterparts that possess a distorted but ordered Cu-S framework. The low μ_H values of the x = 0.075 sample and their temperature dependence can be thus ascribed to the highly-perturbed conductive network formed by CuS_4 tetrahedra due to the cationic Cu/Sn mixed occupation of the 12f site.

The temperature dependence of the total thermal conductivity κ for $Cu_{2.075}Sn_{0.925}S_3$ sample (**Figure 4c**) is comparable to that of Cu_2SnS_3 up to about 50 K, a temperature above which a significant difference between the two samples emerges. The markedly higher values measured in the $x = 0.15$ sample are mostly due to its more conductive nature giving rise to a higher electronic contribution κ_e. At 300 K, the monoclinic phase Cu_2SnS_3 exhibits a relatively low κ value of 1.9 W m^{-1} K^{-1}, which is in line with the value of 2.4 W m^{-1} K^{-1} measured by Shen *et al.* in the series $Cu_2Sn_{1-x}Zn_xS_3$.[1] For the Cu-rich samples, κ increases gradually with increasing the Cu content to reach 4.3 W m^{-1} K^{-1} and 8.6 W m^{-1} K^{-1} at 300 K for the $x = 0.075$ and $x = 0.15$ samples, respectively. The temperature dependence of the lattice thermal conductivity $\kappa_L = \kappa - \kappa_e$ for $Cu_{2.075}Sn_{0.925}S_3$ sample is shown in **Figure 5a**. The electronic thermal conductivity κ_e was calculated using the Wiedemann-Franz law $\kappa_e = \frac{LT}{\rho}$, where L is the Lorenz number. The temperature dependence of L was estimated using a single-parabolic band model with acoustic phonon scattering.[33] It must be noted that the calculated L values for the $x = 0.15$ sample led to unphysical negative values at high temperatures. This inadequacy of the present model to calculate L is due to the multiband nature of the valence band structure of this compound that results in lower L values than those predicted for a highly-degenerate hole gas using the SPB model. This difficulty in determining the lattice contribution has been highlighted in several thermoelectric materials, such as SnTe, for which the presence of several electronic bands tends to lower the L values despite the strongly degenerate nature of the compound.[34–37] The temperature dependence of κ_L for the $x = 0$ sample is characterized by a pronounced Umklapp peak near 50 K followed by a marked decrease with increasing temperature, following approximately a T^{-1} dependence that reflects the dominance of phonon-phonon scattering over other processes. In contrast, the κ_L values of the $x = 0.075$ sample are significantly lower compared to Cu_2SnS_3 below 200 K and remain almost constant across the entire temperature range, strongly departing from the T^{-1} law. The absence of the Umklapp peak is consistent with the reduced cationic order of the $x = 0.075$ sample, evidenced by X-ray diffraction and TEM analyses, and Hall mobility data. This leads to a strong enhancement of point-defect scattering. Such a consideration is supported by the fit of the experimental κ_L data according to the Debye-Callaway model (see equations and references in SI). Within this model, the overall phonon relaxation time is determined by the reciprocal sum of four independent terms describing grain-boundary, point-defect, Umklapp phonon-phonon processes, and normal scattering in the low-temperature limit. The importance of low-energy optical phonons, discussed in **Section 2.4**, was noted also by Deng et al.[5] from the point of view of resonant scattering. The pre-factor of such a contribution is expected to be proportional to the concentration of atoms associated with the low-energy phonon modes and was found to be three orders of magnitude higher than values obtained in skutterudites. Because resonant scattering seems difficult to reconcile with the crystal chemistry of the present compounds, we rather considered normal phonon-phonon processes that can be a significant source of thermal resistance if they dominate the scattering at low temperatures.[38] In the case of Cu_2SnS_3, the normal scattering term was found to be necessary to describe adequately κ_L, with the use of only the first three terms yielding fits of lower quality. As shown in **Figure 5b**, this model describes fairly well the experimental data over the entire temperature range. For Cu_2SnS_3, this model tends to underestimate κ_L above 200 K where effects of radiation losses may contribute. These results (see **Table S3**), nevertheless, show that point-defect scattering is strongly enhanced in the $x = 0.075$ sample. In addition, the manifold of low-energy optical modes in the vibrational spectrum (**Figure 7**) provides a large momentum- and energy-conserving phase space for three-phonon Umklapp scattering involving the acoustic modes.[39–46] These scattering events are thus more easily achieved at low temperatures, further explaining the absence of Umklapp peak in this sample. These results confirm the critical role of partial cationic ordering in limiting the heat transport at low temperatures.

The κ_L value of around 2.0 W m^{-1} K^{-1} at 300 K further decreases to 0.55 W m^{-1} K^{-1} upon warming to 700 K (**Figure 10d**). These remarkably very low values are similar to those inferred in prior studies for disordered Cu-Sn-S phases[1,5] and in other sulfur-based compounds such as tetrahedrites or strongly-disordered colusites.[47–49] At high temperatures, the κ_L values even drop below the minimum lattice thermal conductivity κ_{min} of 0.70 W m^{-1} K^{-1} estimated using the Cahill and Pohl[50] relation $\kappa_{min} = \frac{1}{2}\left(\frac{\pi}{6}\right)^{\frac{1}{3}} k_B V^{-\frac{2}{3}}(2v_T + v_L)$ where V is the average volume per atom, k_B is the Boltzmann constant and $v_T = 2375$ m s^{-1} and $v_L = 4597$ m s^{-1} are the room-temperature transverse and longitudinal sound velocities of $x = 0.075$ sample, respectively. This finding, observed in only few compounds exhibiting ultralow κ_L,[51,52] suggests that the high-temperature lower bound might be better described by atomic vibrations carrying heat by diffusion. In this diffusive regime, the limit κ_{diff} is given by the expression $\kappa_{diff} \approx 0.76 k_B V^{-\frac{2}{3}} \frac{1}{2}(2v_T + v_L)$ yielding $\kappa_{diff} \approx$ 0.45 W m^{-1} K^{-1}, that is, below the inferred κ_L values.[51]

Such low κ_L values for $x = 0.075$ sample lead to *ZT* value of 0.3 at 700K (**Figure 10f**). This maximum *ZT* remains moderate in comparison to those achieved in optimized tetrahedrites and colusites, due to the highly metallic character of $Cu_{2.075}Sn_{0.925}S_3$ sample.[53,54]

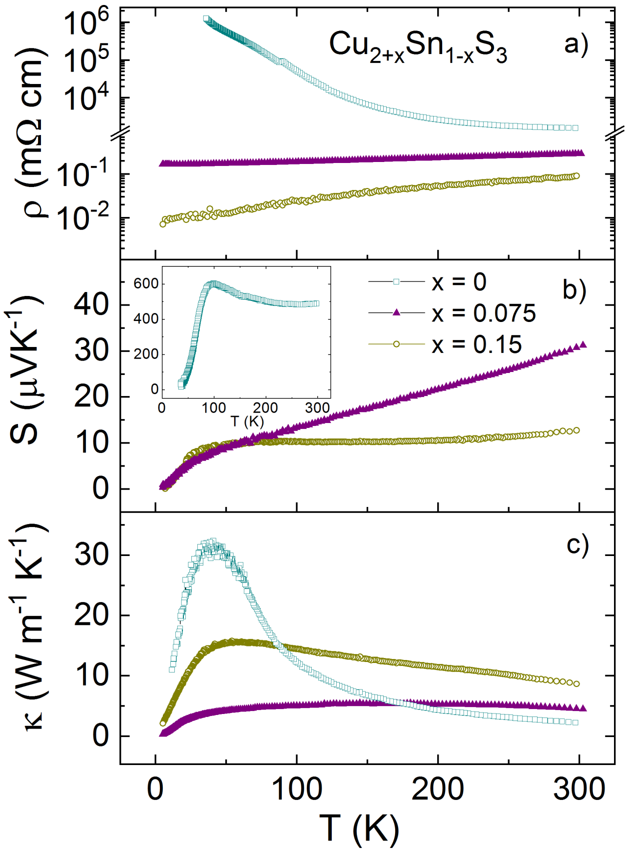

Figure 4. Temperature dependence of (a) electrical resistivity (*ρ*) (b) Seebeck coefficient (*S*), and (c) thermal conductivity (*κ*) from 5 K to 300 K of Cu_2SnS_3, $Cu_{2.075}Sn_{0.925}S_3$ and $Cu_{2.15}Sn_{0.85}S_3$.

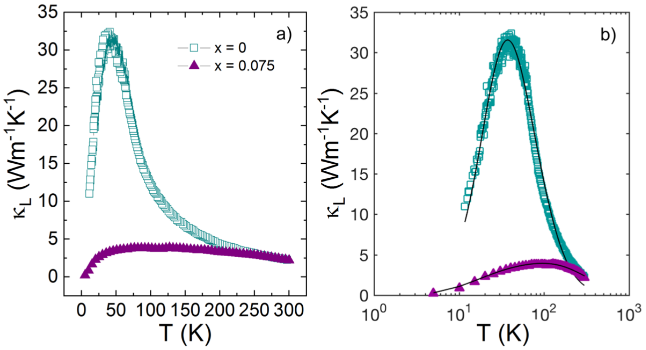

Figure 5. a) Lattice thermal conductivity κ_L from 5 K to 300 K of Cu_2SnS_3 and $Cu_{2.075}Sn_{0.925}S_3$ samples. b) $\kappa_L(T)$ with the solid lines through the experimental data showing the theoretical fits according to the Debye-Callaway model.

3.5. Electronic structure and phonons

In order to properly describe the effect of cationic disorder on the 12f site, three appropriate different arrangements of 8 Cu and 4 Sn were considered and the properties were described in term of integrated average quantities such as the electronic density of states (eDOS, **Figure 6**). Band structures are very sensitive to compositional variations and structural disorder in the CTS family; in $Cu_{22}Sn_{10}S_{32}$ (x = 0.063 in $Cu_{2+x}Sn_{1-x}S_3$) especially, the states filling the pseudo-gap near the Fermi level are in large part associated to Sn on the 12*f* site (**Figure S11**); this site is occupied by Cu and Sn arranged at the vertices of an octahedron in the center and at the corners of the cubic cell in order to minimize the octahedron-octahedron electrostatic repulsion. Analysis of the electron localization factor and charge density (**Figure S12**) points to the local changes in the bonding features in proximity of the 12*f* sites: as expected, the Cu-S bonds are more ionic with respect to the Sn-S bonds.

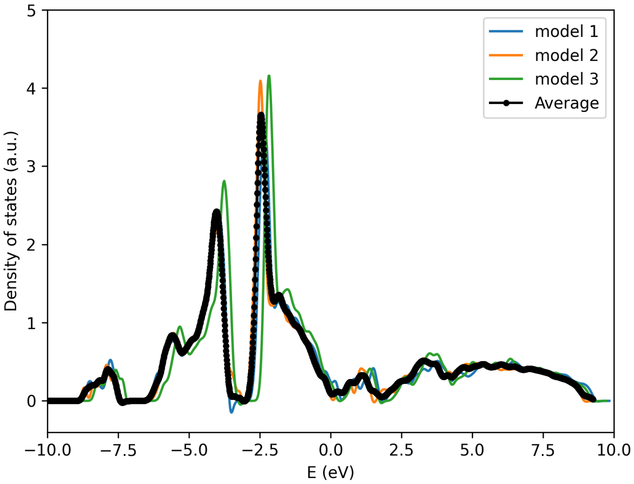

Figure 6. Electron density of states for $Cu_{22}Sn_{10}S_{32}$ ($x = 0.063$ in $Cu_{2+x}Sn_{1-x}S_3$) computed from first principles. Three models have been used to account for the effect of disorder influencing the electronic states near the Fermi level (the energy scale is chosen so that $E_F = 0\ eV$). Plots are

aligned with respect to identical core states. Although the DOS does not exhibit a forbidden energy gap in the proximity of the Fermi level, we used the word "semiconductor" to refer to this material. This is justified by the presence of a pseudo-gap and the temperature dependence of the transport coefficients.

The computed values of the Seebeck coefficient (**Figure S13, left panel**) are in reasonable agreement with the experimental data; the computed electrical resistivity (**Figure S13, right panel**) requires minor changes in the relaxation time to match the low temperature experimental data (**Figure 4a** and **4b**). The comparison between theory and experiments is strongly dependent on the theoretical model used to represent the disorder and the fine tuning of the Fermi energy.

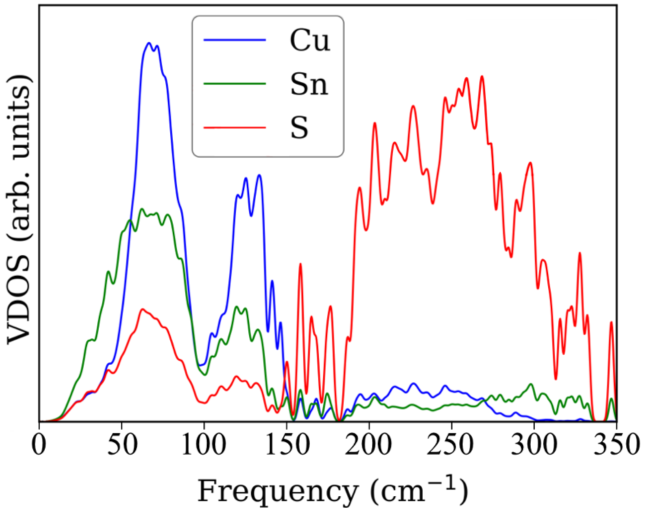

Figure 7. Phonon density of states for $Cu_{22}Sn_{10}S_{32}$ ($x = 0.063$ in $Cu_{2+x}Sn_{1-x}S_3$) computed from first principles. We have used only one model to determine the vibrational spectrum. The main features are similar to those observed in other sulfides.

The vibrational density of states of $Cu_{22}Sn_{10}S_{32}$ (x = 0.063 in $Cu_{2+x}Sn_{1-x}S_3$) is expected to mimic the features observed in other copper sulfides, notably including a low frequency manifold centered at about 60 cm^{-1} involving mostly Cu and Sn displacements (**Figure 7**). The presence of low-energy optical modes were found in several copper-based sulfides with low κ_L.[5,49,55,56] The phonon frequencies have been computed within an accuracy of 2 cm^{-1}.

3.6. $Cu_{22}Sn_{10-y}Sb_yS_{32}$ series

With the aim to decrease the hole concentration while retaining the semi-ordering character of this phase beneficial for suppressing the heat transport, we have investigated the aliovalent substitution of Sb^{5+} for Sn^{4+}, as reported recently in Cu_2SnS_3 and Cu_3SnS_4.[8,57,58] We have fixed the pristine composition to the one determined from synchrotron X-ray diffraction data, *i.e.*, $Cu_{22}Sn_{10}S_{32}$ corresponding to x = 0.063 in the $Cu_{2+x}Sn_{1-x}S_3$ series. For comparison purpose, we also include the thermoelectric properties of x = 0.075 sample.

The XRPD pattern of $Cu_{22}Sn_{10}S_{32}$ (x = 0.063 in $Cu_{2+x}Sn_{1-x}S_3$) clearly shows the diffraction peaks characteristic of a cubic unit cell in space group $P\bar{4}3n$ with a = 10.8322(1) Å (see Rietveld refinement in **Figure S14**). It suggests that there exists a narrow Cu/Sn solubility window (around x = 0.063-0.075) where the mixed occupancy on the 12f site allows to stabilize the cubic $P\bar{4}3n$ crystal structure.

The XRPD patterns of the $Cu_{22}Sn_{10-y}Sb_yS_{32}$ samples with concentration up to y = 1.0 also evidence the diffraction peaks characteristic of the cubic unit cell in space group $P\bar{4}3n$ with a = 10.8350(1) Å and 10.8373(1) Å for y = 0.75 and 1.0, respectively (**Figure 8** and **Figure S14**). Remarkably, such features are absent for y = 1.5 (**Figure 8**), suggesting that this sample crystallizes in tetragonal kuramite structure. This indicates that the stability of the cubic $Cu_{22}Sn_{10}S_{32}$ phase is limited to a narrow Sb concentration range and that transition from cubic $P\bar{4}3n$ structure to tetragonal $I\bar{4}2m$ structure is favored by extra chemical disorder. The absence of extra diffraction peaks other than those allowed by the space group $P\bar{4}3n$ for $y \leq 1$ further suggests a high purity of the $Cu_{22}Sn_{10-y}Sb_yS_{32}$ samples. There is no variation in the peak intensities for $y \leq 1$ consistently with the isoelectronic substitution of Sn^{4+} by Sb^{5+} cations and in agreement with the high quality of Rietveld refinements obtained by considering the structural model determined for the cubic $Cu_{22}Sn_{10}S_{32}$ phase (**Figure S14**). A preferred crystallographic site for the Sb atoms cannot be unequivocally determined from XRPD data only. The refined unit cell parameter of the Sb-containing samples hardly varies upon increasing y, in agreement with the very close ionic radius of Sn^{4+} (0.55 Å) and Sb^{5+} (*i.e.* 0.565 Å) in tetrahedral coordination.[58,59]

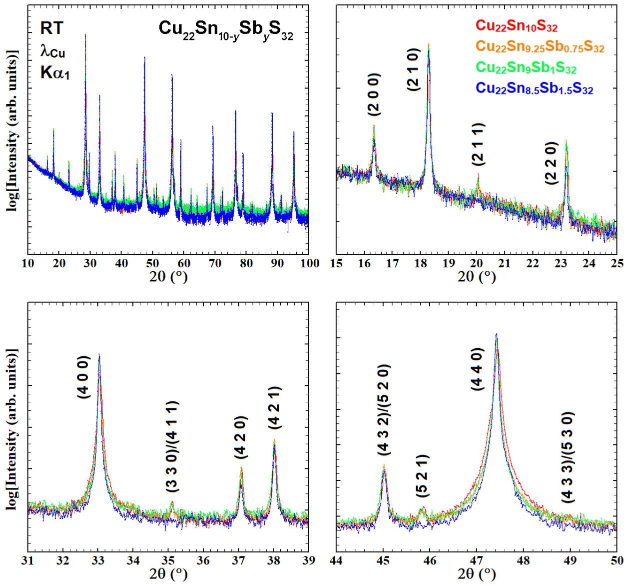

Figure 8. XRPD patterns of the $Cu_{22}Sn_{10-y}Sb_yS_{32}$ samples ($y = 0$ in red, $y = 0.75$ in orange, $y = 1$ in green, and $y = 1.5$ in blue) and Bragg reflections of the cubic $Cu_{22}Sn_{10}S_{32}$ phase ($P\bar{4}3n$, a_c ~10.83 Å).

From a theoretical point of view, the Sb/Sn replacement injects electron into the valence manifold ($22Cu_{Cu}^{X} + 9Sn_{Sn}^{X} + Sb_{Sn}^{\bullet} + 32S_{S}^{X} + e'$) shifting the Fermi level E_F upwards in energy. Due to disorder, few calculations with explicit Sb doping are not representative of the crystal structure determined experimentally. Thus, we opted to treat the doping implicitly within the rigid band and constant relaxation time approximations. **Figure 9** shows the variation of S and σ as E_F changes over a large temperature range, qualitatively capturing the experimental trend (**Figure 10**).

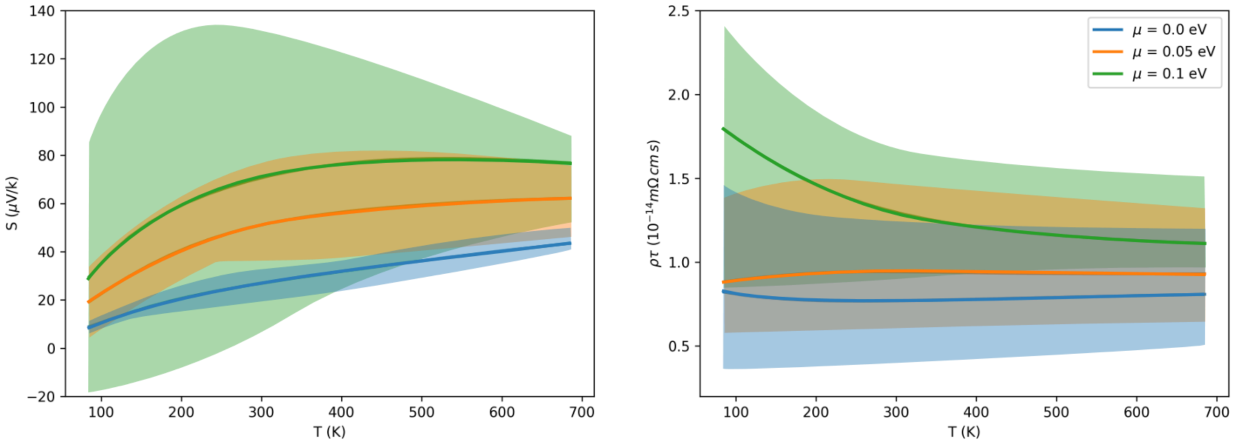

Figure 9. Seebeck coefficient (left) and electrical resistivity (right, multiplied by the constant relaxation time τ) as a function of temperature. The three curves correspond to three different doping levels ($E_F = \mu = 0.0$ eV is the theoretical value for $Cu_{22}Sn_{10}S_{32}$ and is used as energy reference). In the rigid band approximation, shifting up the chemical potential is equivalent to remove holes from the system. We used three different models to simulate disorder: the shaded regions indicate the dispersion of the transport coefficients as the model to represent the Cu-Sn disorder changes; the solid lines indicate the averages.

The transport properties measured between 300 and 700 K are shown in **Figure 10** for the $Cu_{2.075}Sn_{0.925}S_3$ and $Cu_{22}Sn_{10-y}Sb_yS_{32}$ (y = 0, 0.75, and 1.0) compositions. The p-type nature of the parent compound remains unaffected by this substitution. The values of ρ and S, shown in **Figure 10a** and **10b** respectively, increase monotonically with increasing temperature, indicative of degenerate semiconducting behaviors. $Cu_{2.075}Sn_{0.925}S_3$ exhibits the lowest values of $\rho \sim 0.28$ mΩ cm and $S \sim 35$ µV K^{-1} at 300K, consistent with the higher content of copper and its correspondingly higher number of holes compared to the three other compositions investigated. Upon decreasing slightly the Cu content in $Cu_{22}Sn_{10}S_{32}$ ($x = 0.063$ in $Cu_{2+x}Sn_{1-x}S_3$), ρ and S increase to 0.4 mΩ cm and 45 µV K^{-1}, respectively, at 300K. At higher temperatures, the latter remains quite low, $S \sim 97$ µV K^{-1} at 700K, owing to a high hole concentration. The hole concentration remains too high to expect an overall good thermoelectric performance, thus motivating the use of a donor dopant such as Sb in a +5 oxidation state. The existence of pentavalent Sb in tetrahedral coordination is well known in famatinite Cu_3SbS_4 [58] and colusite compounds, as recently reported in $Cu_{26}Ti_2Sb_6S_{32}$ and $Cu_{26}V_2Ge_{6-x}Sb_xS_{32}$.[56] As anticipated, the substitution of Sb for Sn in $Cu_{22}Sn_{10}S_{32}$ results in a significant decrease in the hole concentration, reflected by the simultaneous increase in ρ and S. ρ increases from 0.4 mΩ cm to 0.95 mΩ cm at 300 K, and from 1.0 mΩ cm to 1.9 mΩ cm at 700 K, for $Cu_{22}Sn_{10}S_{32}$ and $Cu_{22}Sn_9SbS_{32}$, respectively.

In order to clarify the role of Sb on the transport properties, Hall effect measurements were carried out. The p-type behavior is confirmed from the positive values of the Hall coefficient. The hole concentration decreases slightly at 300 K with the reduction of copper content, from 4.7×10^{21} cm^{-3} for $Cu_{2.075}Sn_{0.925}S_3$ to 4.2×10^{21} cm^{-3} for $Cu_{22}Sn_{10}S_{32}$ ($x = 0.063$ in $Cu_{2+x}Sn_{1-x}S_3$). With Sb for Sn substitution, the hole concentration decreases to 3.1×10^{21} cm^{-3} for $Cu_{22}Sn_{9.25}Sb_{0.75}S_{32}$ and 1.5×10^{21} cm^{-3} for $Cu_{22}Sn_9SbS_{32}$ in agreement with a nominal change from two to one hole per unit cell. This trend confirms that Sb acts as a donor impurity in these compounds. Concomitantly, μ_H decreases from 4.5 cm^2 V^{-1} s^{-1} for $Cu_{2.075}Sn_{0.925}S_3$ to 3.7 cm^2 V^{-1} s^{-1} for $Cu_{22}Sn_{10}S_{32}$ ($x = 0.063$ in $Cu_{2+x}Sn_{1-x}S_3$) at 300 K. Meanwhile, Sb doping does not seem to strongly impact μ_H with similar values of 3.5 cm^2 V^{-1} s^{-1} and 4.3 cm^2 V^{-1} s^{-1} for $Cu_{22}Sn_{9.25}Sb_{0.75}S_{32}$ and $Cu_{22}Sn_9SbS_{32}$, respectively. Consistent with the decrease in the hole concentration, the S values increase from 45 µV K^{-1} for $Cu_{22}Sn_{10}S_{32}$ to 73 µV K^{-1} for $Cu_{22}Sn_9SbS_{32}$ at 300 K. The peak S value of ~ 147 µV K^{-1} achieved at 700 K for $Cu_{22}Sn_9SbS_{32}$ corresponds to a 51% enhancement compared to pristine $Cu_{22}Sn_{10}S_{32}$.

The temperature dependence of the power factor is shown in **Figure 10e** for the $Cu_{2.075}Sn_{0.925}S_3$ and $Cu_{22}Sn_{10-y}Sb_yS_{32}$ (y = 0, 0.75, and 1.0) compositions. The highest PF is achieved for $Cu_{22}Sn_{9.25}Sb_{0.75}S_{32}$ sample with values ranging from 0.67 mW m^{-1} K^{-2} at 300 K to 1.2 mW m^{-1} K^{-2} at 650 K. This higher value is comparable to that recently reported for $Cu_{2.08}Sn_{0.92}S_3$,[11] *i.e.* 1.26 mW m^{-1} K^{-2} at 700 K and higher than that of Zn- and Co-doped Cu_2SnS_3 (0.84 and 0.94 mW m^{-1} K^{-2} respectively).[1,4]

Figure 10c and **10d** show the temperature dependence of the thermal conductivity κ and lattice thermal conductivity κ_L, respectively, for the $Cu_{2.075}Sn_{0.925}S_3$ and $Cu_{22}Sn_{10-y}Sb_yS_{32}$ (y = 0, 0.75, and 1.0) compositions. $Cu_{2.075}Sn_{0.925}S_3$ exhibits κ value of ~ 4.3 W m^{-1} K^{-1} at 300 K that decreases to ~ 2.5 W m^{-1} K^{-1} upon heating to 700 K. Although quite high, it is worth noting that these values are twice lower than those observed in $Cu_5Sn_2S_7$,[6] in agreement with the existence of intrinsic partial disorder in the cubic $P\bar{4}3n$ structure. In the case of $Cu_{22}Sn_{10}S_{32}$ ($x = 0.063$ in $Cu_{2+x}Sn_{1-x}S_3$), the κ value decreases from 3.5 W m^{-1} K^{-1} at 300 K to 2.0 W m^{-1} K^{-1} at 700 K. κ further decreases with increasing the Sb content, reaching the lowest value of 1.47 W m^{-1} K^{-1} at 700 K for $Cu_{22}Sn_9SbS_{32}$. This reduction in κ is mainly caused by a decrease in the electronic contribution κ_e. For all the compositions, κ_L roughly follows a T^{-1} dependence, which indicates that Umklapp scattering is the main source of phonon scattering, consistent with the low-temperature measurements. κ_L values for $Cu_{2.075}Sn_{0.925}S_3$, $Cu_{22}Sn_{10}S_{32}$, and $Cu_{22}Sn_{9.25}Sb_{0.75}S_{32}$ fall within the same range, between 1.95 and 1.80 W m^{-1} K^{-1} at 300 K. κ_L does not seem to vary significantly with the Sb content due to the similar molar mass and ionic radii that result in a marginal enhancement of point defect scattering. In contrast, $Cu_{22}Sn_9SbS_{32}$ exhibits slightly higher values of κ_L over the entire temperature range that could be attributed to the presence of larger grains compared to the other compositions, as observed by SEM (**Figure S15**). Conversely, $Cu_{2.075}Sn_{0.925}S_3$ exhibits the lowest κ_L of 0.5 W m^{-1} K^{-1} at 700 K, which is quite comparable with the structurally-similar compounds such as disordered Zn-doped Cu_2SnS_3, $Cu_{2.1}Sn_{0.9}S_3$ (reported as $Cu_7Sn_3S_{10}$), and colusites $Cu_{26}T_2M_6S_{32}$ (T = V, Nb, Ta, Cr, Mo, W; M = Ge, Sn).[1,5,60]

The temperature dependence of ZT for the $Cu_{2.075}Sn_{0.925}S_3$ and $Cu_{22}Sn_{10-y}Sb_yS_{32}$ (y = 0, 0.75, and 1.0) compositions is shown in **Figure 10f**. ZT values increase monotonically for all the compositions with increasing temperature and increase significantly with Sb substitution. The $Cu_{22}Sn_9SbS_{32}$ sample exhibits the highest peak ZT value of 0.55 at 700 K, which is nearly almost twice as high as the ZT value of $Cu_{2.075}Sn_{0.925}S_3$, and similar to those measured in Zn and Co-doped Cu_2SnS_3 and $Cu_{2.1}Sn_{0.9}S_3$ (reported as $Cu_7Sn_3S_{10}$).[1,4,5] Such relatively high ZT value originates from the combination of low lattice thermal conductivity and high power factor further optimized through electron doping with Sb^{5+}.

In order to estimate the optimum hole carrier concentration range, the theoretical hole concentration (p) dependence of ZT has been calculated by using SPB model, as shown in **Figure 11**. The predicted optimal carrier concentration corresponding to the maximum ZT is around 5.0×10^{20} cm^{-3} at 600 K. The optimized values are lower than experimentally measured hole carrier concentration values in the present study, indicating that there is a large room for further improvement of ZT values. In order to achieve such optimum values, careful selection of appropriate substituent element is necessary. Local disorder must be maintained on the 12f site of the cubic $P\bar{4}3n$ structure, while maintaining high mobility in the Cu-S conducting network. As shown in structurally-related colusites,[49,61] a fine tuning of the cationic and/or anionic stoichiometries can promote strong phonon scattering through cationic disorder while tuning the carrier concentration and preserving high power factors. This led to record *ZT* values in sulfides. Enhanced disorder and optimized hole concentrations and *ZT* have been also recently achieved in $Cu_{2.1}Sn_{0.9}S_3$ (reported as $Cu_7Sn_3S_{10}$) through electron doping with Cl and Br.[62]

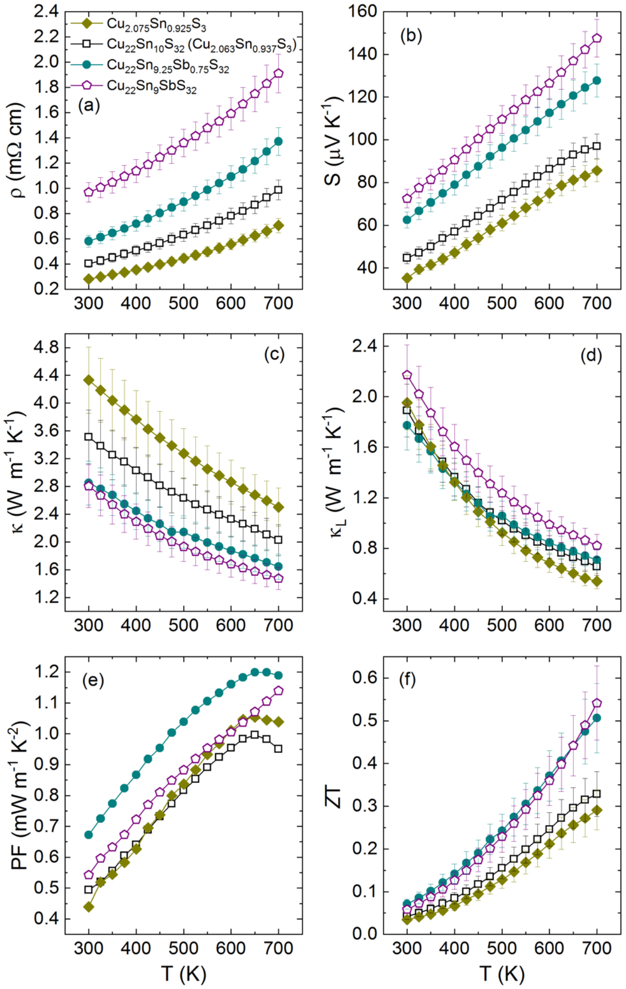

Figure 10. The thermoelectric performances of $Cu_{2.075}Sn_{0.925}S_3$ and $Cu_{22}Sn_{10\text{-}y}Sb_yS_{32}$ (y = 0, 0.75, and 1.0) including (a) electrical resistivity, (b) Seebeck coefficient, (c) thermal conductivity, (d) lattice thermal conductivity, (e) power factor and (f) figure of merit, *ZT*.

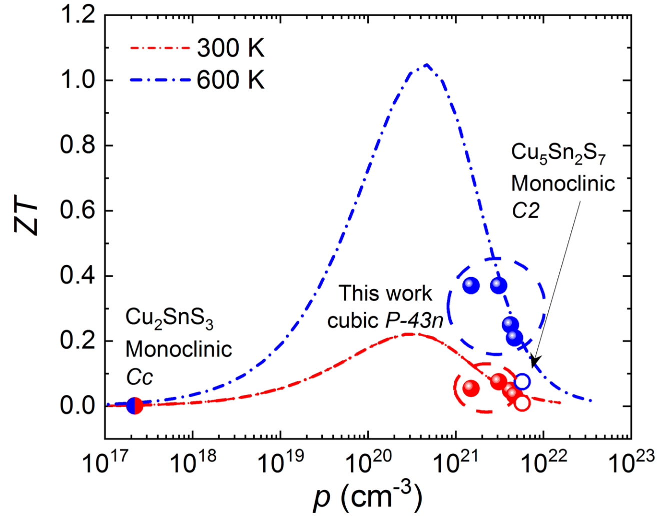

Figure 11. Theoretical hole concentration (p) dependence of ZT at 300 and 600 K for the series $Cu_{22}Sn_{10-y}Sb_yS_{32}$ (y = 0, 0.75, and 1.0; filled circle symbols). For comparison, the data of monoclinic Cu_2SnS_3 (filled bicolor symbol) and $Cu_5Sn_2S_7$ (open circle symbols) have been included. The two dashed curves show the estimated ZT values calculated using the SPB model based on the experimental data (see SI).

4. Conclusion

We have discovered and characterized a new phase in the Cu-Sn-S diagram, namely cubic $P\bar{4}3n$ $Cu_{22}Sn_{10}S_{32}$, which exhibits an original crystallographic structure characterized by local disorder solely on the 12*f* crystallographic site. We have justified the origin of such feature in terms of electrostatic repulsion and investigated the interplay between partial disorder and electronic and thermal transport properties. The extremely low thermal conductivity invites further optimization, successfully realized through the partial substitution of Sb for Sn. The resulting decrease in the hole concentration drives the drastic enhancement of the thermoelectric performance by increasing power factor. ZT values up to 0.55 at 700 K were obtained thanks to electronic optimization that mainly lowers the electronic part of the thermal conductivity. The analysis with multiple characterization methods and modelling further clarifies the sensitivity of materials in the Cu-Sn-S family to minor changes in the chemical composition and disorder and will provide new perspectives for the design of CTS materials for energy applications.

ASSOCIATED CONTENT

Supporting Information

The Supporting Information is available free of charge at XXXXX.

Synchrotron XRPD patterns, temperature dependence of carrier concentration and mobility, Site projected electronic density of states in the proximity of the Fermi level, Charge density and electron localization function (ELF), computed Seebeck coefficient (left) and electrical resistivity, SEM micrographs, crystallographic data from refinement of the single cristal X-ray diffraction data, Equations for the Debye-Callaway model used to fit the lattice thermal conductivity, Equations for the single-parabolic band (SPB) model.

AUTHOR INFORMATION

Corresponding Author

Emmanuel Guilmeau, emmanuel.guilmeau@ensicaen.fr,

Pierric Lemoine, pierric.lemoine@univ-rennes1.fr

Marco Fornari, marco.fornari@cmich.edu

Author Contributions

The manuscript was written through contributions of all authors. All authors have given approval to the final version of the manuscript.

Funding Sources

French Agence Nationale de la Recherche LabEx EMC3 through the Project FACTO (Grant No. ANR-10-LABX-09-01)

Notes

The authors declare no conflict of interest.

ACKNOWLEDGMENTS

The authors gratefully thank Christelle Bilot, Jerôme Lecourt, Vincent Dorcet, Francis Gouttefangeas and Loïc Joanny for technical support. The authors acknowledge SOLEIL for provision of synchrotron radiation facilities, CDIFX for single-crystal X-ray diffraction facilities and CMEBA (platform of the ScanMAT unit, UMS 2001, University of Rennes 1) for scanning electron microscopy with energy dispersive spectroscopy analyses. The authors acknowledge the financial support of the French Agence Nationale de la Recherche LabEx EMC3 through the Project FACTO (Grant No. ANR-10-LABX-09-01), the Normandy Region (Réseau d'Intérêt Normand - Label d'excellence), CARNOT ESP and FEDER.

Crystallographic data

Further details of the crystal structure investigations of $Cu_{22}Sn_{10}S_{32}$ may be obtained from FIZ Karlsruhe, 76344 Eggenstein-Leopoldshafen, Germany (fax: (+49)7247−808−666; e-mail: crysdata@fiz-karlsruhe.de), on quoting the deposition number CSD-2088387.

References:

(1) Shen, Y.; Li, C.; Huang, R.; Tian, R.; Ye, Y.; Pan, L.; Koumoto, K.; Zhang, R.; Wan, C.; Wang, Y. Eco-Friendly p-Type Cu_2SnS_3 Thermoelectric Material: Crystal Structure and Transport Properties. *Sci. Rep.* **2016**, *6*, 32501.

(2) Lokhande, A. C.; Babar, P. T.; Karade, V. C.; Gang, M. G.; Lokhande, V. C.; Lokhande, C. D.; Kim, J. H. The Versatility of Copper Tin Sulfide. *J. Mater. Chem. A* **2019**, *7* (29), 17118–17182.

(3) Lemoine, P.; Guélou, G.; Raveau, B.; Guilmeau, E. Crystal Structure Classification of Copper-Based Sulphides as a Tool for the Design of Inorganic Functional Materials. *Angew. Chemie - Int. Ed.* **2021**. https://doi.org/10.1002/anie.202108686

(4) Zhao, H.; Xu, X.; Li, C.; Tian, R.; Zhang, R.; Huang, R.; Lyu, Y.; Li, D.; Hu, X.; Pan, L.; Wang, Y. Cobalt-Doping in Cu_2SnS_3: Enhanced Thermoelectric Performance by Synergy of Phase Transition and Band Structure Modification. *J. Mater. Chem. A* **2017**, *5* (44), 23267–23275.

(5) Deng, T.; Xing, T.; Brod, M. K.; Sheng, Y.; Qiu, P.; Veremchuk, I.; Song, Q.; Wei, T.-R.; Yang, J.; Snyder, G. J.; Grin, Y.; Chen, L.; Shi, X. Discovery of High-Performance Thermoelectric Copper Chalcogenide Using Modified Diffusion-Couple High-Throughput Synthesis and Automated Histogram Analysis Technique. *Energy Environ. Sci.* **2020**, *13* (9), 3041–3053.

(6) Pavan Kumar, V.; Lemoine, P.; Carnevali, V.; Guélou, G.; Lebedev, O. I.; Boullay, P.; Raveau, B.; Al Rahal Al Orabi, R.; Fornari, M.; Prestipino, C.; Menut, D.; Candolfi, C.; Malaman, B.; Juraszek, J.; Guilmeau, E. Ordered Sphalerite Derivative $Cu_5Sn_2S_7$: A

Degenerate Semiconductor with High Carrier Mobility in the Cu-Sn-S Diagram. *J. Mater. Chem. A* **2021**, *9*, 10812–10826.

(7) Yang, Y.; Ying, P.; Wang, J.; Liu, X.; Du, Z.; Chao, Y.; Cui, J. Enhancing the Thermoelectric Performance of Cu_3SnS_4-Based Solid Solutions through Coordination of the Seebeck Coefficient and Carrier Concentration. *J. Mater. Chem. A* **2017**, *5* (35), 18808–18815.

(8) Chen, K.; Di Paola, C.; Laricchia, S.; Reece, M. J.; Weber, C.; McCabe, E.; Abrahams, I.; Bonini, N. Structural and Electronic Evolution in the Cu_3SbS_4-Cu_3SnS_4 Solid Solution. *J. Mater. Chem. C* **2020**, *8* (33), 11508–11516.

(9) Chen, X.; Wada, H.; Sato, A.; Mieno, M. Synthesis, Electrical Conductivity, and Crystal Structure of $Cu_4Sn_7S_{16}$ and Structure Refinement of Cu_2SnS_3. *J. Solid State Chem.* **1998**, *139* (139), 144–151.

(10) Onoda, M.; Chen, X.; Sato, A.; Wada, H. Crystal Structure and Twinning of Monoclinic Cu_2SnS_3. *Mater. Res. Bull.* **2000**, *35* (9), 1563–1570.

(11) Deng, T.; Qiu, P.; Song, Q.; Chen, H.; Wei, T.; Chen, L.; Xi, L.; Shi, X.; Chen, L. Thermoelectric Properties of Non-Stoichiometric $Cu_{2+x}Sn_{1-x}S_3$. *J. Appl. Phys.* **2019**, *126*, 085111.

(12) Goto, Y.; Naito, F.; Sato, R.; Yoshiyasu, K.; Itoh, T.; Kamihara, Y.; Matoba, M. Enhanced Thermoelectric Figure of Merit in Stannite–Kuramite Solid Solutions $Cu_{2+x}Fe_{1-x}SnS_{4-y}$ (x = 0–1) with Anisotropy Lowering. *Inorg. Chem.* **2013**, *52* (17), 9861–9866.

(13) Tiwari, D.; Chaudhuri, T. K.; Shripathi, T.; Deshpande, U. Synthesis of Earth-Abundant Cu_2SnS_3 Powder Using Solid State Reaction. *J. Phys. Chem. Solids* **2014**, *75* (3), 410–415.

(14) Goto, Y.; Sakai, Y.; Kamihara, Y.; Matoba, M. Electronic Structure and Transport Properties of Cu-Deficient Kuramite $Cu_{3-x}SnS_4$. *Jpn. J. Appl. Phys.* **2015**, *54* (2), 21801.

(15) Schäfer, W.; Scheunemann, K.; Nitsche, R. Crystal Structure and Magnetic Properties of $Cu_4NiSi_2S_7$. *Mater. Res. Bull.* **1980**, *15* (7), 933–937.

(16) Fan, J.; Carrillo-cabrera, W.; Antonyshyn, I.; Prots, Y.; Veremchuk, I.; Schnelle, W.; Drathen, C.; Chen, L.; Grin, Y. Crystal Structure and Physical Properties of Ternary Phases around the Composition $Cu_5Sn_2Se_7$ with Tetrahedral Coordination of Atoms. **2014**, *26* (18), 5244–5251.

(17) Sitaud, B.; Solari, P. L.; Schlutig, S.; Llorens, I.; Hermange, H. Characterization of Radioactive Materials Using the MARS Beamline at the Synchrotron SOLEIL. *J. Nucl. Mater.* **2012**, *425* (1), 238–243.

(18) Rodríguez-Carvajal, J. Recent Advances in Magnetic Structure Determination by Neutron Powder Diffraction. *Phys. B Condens. Matter* **1993**, *192* (1–2), 55–69.

(19) Roisnel, T.; Rodríguez-Carvajal, J. WinPLOTR: A Windows Tool for Powder Diffraction Patterns Analysis. *Mater. Sci. Forum* **2001**, *378–381*, 118–123.

(20) Altomare, A.; Burla, M. C.; Camalli, M.; Cascarano, G. L.; Giacovazzo, C.; Guagliardi, A.; Moliterni, A. G. G.; Polidori, G.; Spagna, R. SIR97: A New Tool for Crystal Structure Determination and Refinement. *J. Appl. Crystallogr.* **1999**, *32* (1), 115–119.

(21) Sheldrick, G. M. Crystal Structure Refinement with SHELXL. *Acta Crystallogr. Sect. C* **2015**, *71* (1), 3–8.

(22) Farrugia, L. J. WinGX and ORTEP for Windows: An Update. *J. Appl. Crystallogr.* **2012**,

45 (4), 849–854.

(23) Alleno, E.; Bérardan, D.; Byl, C.; Candolfi, C.; Daou, R.; Decourt, R.; Guilmeau, E.; Hébert, S.; Hejtmanek, J.; Lenoir, B.; Masschelein, P.; Ohorodnichuk, V.; Pollet, M.; Populoh, S.; Ravot, D.; Rouleau, O.; Soulier, M. A Round Robin Test of the Uncertainty on the Measurement of the Thermoelectric Dimensionless Figure of Merit of $Co_{0.97}Ni_{0.03}Sb_3$. *Rev. Sci. Instrum.* **2015**, *86*, 011301.

(24) Giannozzi, P.; Baroni, S.; Bonini, N.; Calandra, M.; Car, R.; Cavazzoni, C.; Ceresoli, D.; Chiarotti, G. L.; Cococcioni, M.; Dabo, I.; Dal Corso, A.; de Gironcoli, S. QUANTUM ESPRESSO : A Modular and Open-Source Software Project for Quantum Simulations of Materials. *J. Phys. Condens. Matter* **2009**, *21*, 395502.

(25) Supka, A. R.; Lyons, T. E.; Liyanage, L.; D'Amico, P.; Al Rahal Al Orabi, R.; Mahatara, S.; Gopal, P.; Toher, C.; Ceresoli, D.; Calzolari, A.; Curtarolo, S.; Nardelli, M. B.; Fornari, M. AFLOWπ: A Minimalist Approach to High-Throughput Ab Initio Calculations Including the Generation of Tight-Binding Hamiltonians. *Comput. Mater. Sci.* **2017**, *136*, 76–84.

(26) Hamann, D. R. Optimized Norm-Conserving Vanderbilt Pseudopotentials. *Phys. Rev. B* **2013**, *88* (8), 85117.

(27) Agapito, L. A.; Curtarolo, S.; Nardelli, M. B. Reformulation of DFT + U as a Pseudohybrid Hubbard Density Functional for Accelerated Materials Discovery. *Phys. Rev. X* **2015**, *5*, 011006.

(28) Prandini, G.; Marrazzo, A.; Castelli, I. E.; Mounet, N.; Marzari, N. Precision and Efficiency in Solid-State Pseudopotential Calculations. *npj Comput. Mater.* **2018**, *4* (1),

72.

(29) Buongiorno Nardelli, M.; Cerasoli, F. T.; Costa, M.; Curtarolo, S.; De Gennaro, R.; Fornari, M.; Liyanage, L.; Supka, A. R.; Wang, H. PAOFLOW: A Utility to Construct and Operate on Ab Initio Hamiltonians from the Projections of Electronic Wavefunctions on Atomic Orbital Bases, Including Characterization of Topological Materials. *Comput. Mater. Sci.* **2018**, *143*, 462–472.

(30) Harrison, J. W.; Hauser, J. R. Alloy Scattering in Ternary III-V Compounds. *Phys. Rev. B* **1976**, *13* (12), 5347–5350.

(31) Xie, H.; Wang, H.; Fu, C.; Liu, Y.; Snyder, G. J.; Zhao, X.; Zhu, T. The Intrinsic Disorder Related Alloy Scattering in ZrNiSn Half-Heusler Thermoelectric Materials. *Sci. Rep.* **2014**, *4* (1), 6888.

(32) Ibrahim, D.; Candolfi, C.; Migot, S.; Ghanbaja, J.; Dauscher, A.; Le Caër, G.; Malaman, B.; Semprimoschnig, C.; Lenoir, B. Comprehensive Study of the Low-Temperature Transport Properties of Polycrystalline $Sn_{1+x}Te$ (x =0 and 0.03). *Phys. Rev. Mater.* **2019**, *3* (8), 85404.

(33) Fistul, V. I. *Heavily Doped Semiconductors, Plenum Press, New York*, Plenum Pre.; 1969.

(34) McKinney, R. W.; Gorai, P.; Stevanović, V.; Toberer, E. S. Search for New Thermoelectric Materials with Low Lorenz Number. *J. Mater. Chem. A* **2017**, *5*, 17302–17311.

(35) Thesberg, M.; Kosina, H.; Neophytou, N. On the Lorenz Number of Multiband Materials. *Phys. Rev. B* **2017**, *95* (12), 125206.

(36) Prokof'eva, L. V.; Shabaldin, A. A.; Korchagin, V. A.; Nemov, S. A.; Ravich, Y. I. Lorentz Number and Hall Factor in Degenerate Semiconductors during Resonance Scattering of Charge Carriers. *Semiconductors* **2008**, *42*, 1161.

(37) Misra, S.; Wiendlocha, B.; Tobola, J.; Fesquet, F.; Dauscher, A.; Lenoir, B.; Candolfi, C. Band Structure Engineering in $Sn_{1.03}Te$ through an In-Induced Resonant Level. *J. Mater. Chem. C* **2020**, *8* (3), 977–988.

(38) Ward, A.; Broido, D. A. Intrinsic Phonon Relaxation Times from First-Principles Studies of the Thermal Conductivities of Si and Ge. *Phys. Rev. B* **2010**, *81* (8), 85205.

(39) Viennois, R.; Koza, M. M.; Debord, R.; Toulemonde, P.; Mutka, H.; Pailhès, S. Anisotropic Low-Energy Vibrational Modes as an Effect of Cage Geometry in the Binary Barium Silicon Clathrate $Ba_{24}Si_{100}$. *Phys. Rev. B* **2020**, *101* (22), 224302.

(40) Pailhès, S.; Euchner, H.; Giordano, V. M.; Debord, R.; Assy, A.; Gomès, S.; Bosak, A.; Machon, D.; Paschen, S.; de Boissieu, M. Localization of Propagative Phonons in a Perfectly Crystalline Solid. *Phys. Rev. Lett.* **2014**, *113* (2), 25506.

(41) H. Lee, C.; Hase, I.; Sugawara, H.; Yoshizawa, H.; Sato, H. Low-Lying Optical Phonon Modes in the Filled Skutterudite $CeRu_4Sb_{12}$. *J. Phys. Soc. Japan* **2006**, *75* (12), 123602.

(42) Jana, M. K.; Pal, K.; Warankar, A.; Mandal, P.; Waghmare, U. V; Biswas, K. Intrinsic Rattler-Induced Low Thermal Conductivity in Zintl Type $TlInTe_2$. *J. Am. Chem. Soc.* **2017**, *139* (12), 4350–4353.

(43) Dutta, M.; Matteppanavar, S.; Prasad, M. V. D.; Pandey, J.; Warankar, A.; Mandal, P.; Soni, A.; Waghmare, U. V; Biswas, K. Ultralow Thermal Conductivity in Chain-like TlSe Due to Inherent Tl+ Rattling. *J. Am. Chem. Soc.* **2019**, *141* (51), 20293–20299.

(44) Tadano, T.; Tsuneyuki, S. Quartic Anharmonicity of Rattlers and Its Effect on Lattice Thermal Conductivity of Clathrates from First Principles. *Phys. Rev. Lett.* **2018**, *120* (10), 105901.

(45) Misra, S.; Barreteau, C.; Crivello, J.-C.; Giordano, V. M.; Castellan, J.-P.; Sidis, Y.; Levinský, P.; Hejtmánek, J.; Malaman, B.; Dauscher, A.; Lenoir, B.; Candolfi, C.; Pailhès, S. Reduced Phase Space of Heat-Carrying Acoustic Phonons in Single-Crystalline InTe. *Phys. Rev. Res.* **2020**, *2* (4), 43371.

(46) Bouyrie, Y.; Candolfi, C.; Pailhès, S.; Koza, M. M.; Malaman, B.; Dauscher, A.; Tobola, J.; Boisron, O.; Saviot, L.; Lenoir, B. From Crystal to Glass-like Thermal Conductivity in Crystalline Minerals. *Phys. Chem. Chem. Phys.* **2015**, *17* (30), 19751–19758.

(47) Lu, X.; Morelli, D. T.; Xia, Y.; Zhou, F.; Ozolins, V.; Chi, H.; Zhou, X.; Uher, C. High Performance Thermoelectricity in Earth-Abundant Compounds Based on Natural Mineral Tetrahedrites. *Adv. Energy Mater.* **2013**, *3*, 342–348.

(48) Suekuni, K.; Tsuruta, K.; Kunii, M.; Nishiate, H.; Nishibori, E.; Maki, S.; Ohta, M.; Yamamoto, A.; Koyano, M. High-Performance Thermoelectric Mineral $Cu_{12-x}Ni_xSb_4S_{13}$ Tetrahedrite. *J. Appl. Phys.* **2013**, *113*, 043712.

(49) Bourgès, C.; Bouyrie, Y.; Supka, A. R.; Al Rahal Al Orabi, R.; Lemoine, P.; Lebedev, O. I.; Ohta, M.; Suekuni, K.; Nassif, V.; Hardy, V.; Daou, R.; Miyazaki, Y.; Fornari, M.; Guilmeau, E. High-Performance Thermoelectric Bulk Colusite by Process Controlled Structural Disordering. *J. Am. Chem. Soc.* **2018**, *140* (6), 2186–2195.

(50) Cahill, D. G.; Watson, S. K.; Pohl, R. O. Lower Limit to the Thermal Conductivity of Disordered Crystals. *Phys. Rev. B* **1992**, *46*, 6131–6140.

(51) Agne, M. T.; Hanus, R.; Snyder, G. J. Minimum Thermal Conductivity in the Context of Diffuson-Mediated Thermal Transport. *Energy Environ. Sci.* **2018**, *11* (3), 609–616.

(52) Misra, S.; Levinský, P.; Dauscher, A.; Medjahdi, G.; Hejtmánek, J.; Malaman, B.; Snyder, G. J.; Lenoir, B.; Candolfi, C. Synthesis and Physical Properties of Single-Crystalline InTe: Towards High Thermoelectric Performance. *J. Mater. Chem. C* **2021**, *9* (15), 5250–5260.

(53) Lu, X.; Morelli, D. T.; Xia, Y.; Ozolins, V. Increasing the Thermoelectric Figure of Merit of Tetrahedrites by Co-Doping with Nickel and Zinc. *Chem. Mater.* **2015**, *27* (2), 408–413.

(54) Bouyrie, Y.; Ohta, M.; Suekuni, K.; Kikuchi, Y.; Jood, P.; Yamamoto, A.; Takabatake, T. Enhancement in the Thermoelectric Performance of Colusites $Cu_{26}A_2E_6S_{32}$(A = Nb, Ta; E = Sn, Ge) Using E-Site Non-Stoichiometry. *J. Mater. Chem. C* **2017**, *5* (17), 4174–4184.

(55) Pavan Kumar, V.; Supka, A. R.; Lemoine, P.; Lebedev, O. I.; Raveau, B.; Suekuni, K.; Nassif, V.; Al Rahal Al Orabi, R.; Fornari, M.; Guilmeau, E. High Power Factors of Thermoelectric Colusites $Cu_{26}T_2Ge_6S_{32}$ (T = Cr, Mo, W): Toward Functionalization of the Conductive “Cu–S” Network. *Adv. Energy Mater.* **2019**, *9* (0), 1803249.

(56) Hagiwara, T.; Suekuni, K.; Lemoine, P.; Supka, A. R.; Chetty, R.; Guilmeau, E.; Raveau, B.; Fornari, M.; Ohta, M.; Al Rahal Al Orabi, R.; Saito, H.; Hashikuni, K.; Ohtaki, M. Key Role of d^0 and d^{10} Cations for the Design of Semiconducting Colusites: Large Thermoelectric ZT in $Cu_{26}Ti_2Sb_6S_{32}$ Compounds. *Chem. Mater.* **2021**, *33*, 3449.

(57) Zhao, Y.; Gu, Y.; Zhang, P.; Hu, X.; Wang, Y.; Zong, P.; Pan, L.; Lyu, Y.; Koumoto, K. Enhanced Thermoelectric Performance in Polymorphic Heavily Co-Doped Cu_2SnS_3 through Carrier Compensation by Sb Substitution. *Sci. Technol. Adv. Mater.* **2021**, *22*,

363.

(58) Chen, K.; Di Paola, C.; Du, B.; Zhang, R.; Laricchia, S.; Bonini, N.; Weber, C.; Abrahams, I.; Yan, H.; Reece, M. Enhanced Thermoelectric Performance of Sn-Doped Cu_3SbS_4. *J. Mater. Chem. C* **2018**, *6*, 8546–8552.

(59) Shannon, R. D. Revised Effective Ionic Radii and Systematic Studies of Interatomic Distances in Halides and Chalcogenides. *Acta Crystallogr. Sect. A* **1976**, *32*, 751–767.

(60) Guélou, G.; Lemoine, P.; Raveau, B.; Guilmeau, E. Recent Developments in High-Performance Thermoelectric Sulphides: An Overview of the Promising Synthetic Colusites. *J. Mater. Chem. C* **2021**, *9*, 773–795.

(61) Suekuni, K.; Shimizu, Y.; Nishibori, E.; Kasai, H.; Saito, H.; Yoshimoto, D.; Hashikuni, K.; Bouyrie, Y.; Chetty, R.; Ohta, M.; Guilmeau, E.; Takabatake, T.; Watanabe, K.; Ohtaki, M. Atomic-Scale Phonon Scatterers in Thermoelectric Colusites with a Tetrahedral Framework Structure. *J. Mater. Chem. A* **2019**, *7*, 228–235.

(62) Deng, T.; Qiu, P.; Xing, T.; Zhou, Z.; Wei, T. R.; Ren, D.; Xiao, J.; Shi, X.; Chen, L. A Low-Cost and Eco-Friendly Br-Doped $Cu_7Sn_3S_{10}$ Thermoelectric Compound with ZT around Unity. *J. Mater. Chem. A* **2021**, *9* (12), 7946–7954.

For Table of Contents Only

We have discovered a new partially-ordered cubic $Cu_{22}Sn_{10}S_{32}$ phase in the Cu-Sn-S diagram with intrinsically low lattice thermal conductivity. Our results provide new perspectives for the design of copper-based chalcogenides for energy applications.